

How Does the Eye Warm? Part I: A Potential Temperature Budget Analysis of an Idealized Tropical Cyclone

DANIEL P. STERN AND FUQING ZHANG

Department of Meteorology, The Pennsylvania State University, University Park, Pennsylvania

(Manuscript received 5 December 2011, in final form 7 August 2012)

ABSTRACT

In this first part of a two-part study, the mechanisms that accomplish the warming in the eye of tropical cyclones are investigated through a potential temperature budget analysis of an idealized simulation. The spatial structure of warming varies substantially with time. During rapid intensification (RI), the warming is maximized at midlevels, and as a consequence, the perturbation temperature is always maximized in this region.

At the start of RI, total advection of potential temperature is the only significant term contributing to warming the eye. However, for a substantial portion of RI, the region of most rapid warming actually undergoes mean ascent. The net advective warming is shown to be a result of eddy radial advection of potential temperature, dominated by a wavenumber-1 feature that is likely due to a dynamic instability. At a sufficient intensity, mean vertical advective warming becomes concentrated in a narrow zone just inward of the eyewall. In agreement with prior studies, this advective tendency is largely canceled by diabatic cooling. Subgrid-scale horizontal diffusion of potential temperature plays a surprisingly large role in the maintenance of the warm-core structure, and when the storm is intense, yields a negative tendency that can be of the same magnitude as advective warming.

1. Introduction

A defining characteristic of tropical cyclones is that they are warmer than their environment throughout most of the depth of the troposphere. As such, they are referred to as “warm-core” vortices. To a first approximation, tropical cyclones are in thermal wind balance (Willoughby 1990), and so this warm core is associated with the strength of the primary circulation (i.e., the tangential winds) decreasing with height above the top of the boundary layer (where a maximum is generally found; e.g., Franklin et al. 2003).¹ These characteristics have been known for many years, and there are numerous

studies that comment in some manner on the warm-core nature of tropical cyclones. Given this, surprisingly little is known about the details of the warm core, including the height at which it is most typically maximized, the variability of this height with intensity, size, and environment, and even the mechanisms by which the warming is accomplished. This is primarily for two reasons: in situ mid- and upper-tropospheric observations of tropical cyclones are very rare in the last 40 yr, and a few early case studies from the 1960s and 1970s (La Seur and Hawkins 1963; Hawkins and Rubsam 1968; Hawkins and Imbembo 1976) have dominated many scientists viewpoints regarding the warm core, leading to the misperception that much more is known than is actually the case, as shown in Stern and Nolan (2012, hereafter SN12). SN12 further showed that in idealized numerical simulations, the warm core was generally maximized in the midtroposphere (4–8 km), in contrast to what is widely believed to be a preferred upper-tropospheric (above 10 km) maximum (Halverson et al. 2006; Holland 1997; Knaff et al. 2004; Braun 2002; Emanuel 1986; Wang 2001; Powell et al. 2009). In this study, we continue to investigate the mean structure and variability of the warm core in numerical simulations,

¹ Note that the rapid decrease of tangential winds with height in the (~1 km) layer just above the maximum is not a consequence of the warm-core nature of tropical cyclones. Rather, it is associated with the height variation of unbalanced flow (Kepert 2001; Stern and Nolan 2011).

Corresponding author address: Dr. Daniel P. Stern, Department of Meteorology, The Pennsylvania State University, University Park, PA 16802.
E-mail: dps19@psu.edu

and examine the mechanisms by which this structure is achieved, through analysis of a potential temperature budget.

At a fundamental level, a warm core exists because there is a negative radial gradient of equivalent potential temperature θ_e in the boundary layer, associated with a negative radial gradient in surface fluxes, which are ultimately responsible for the genesis, intensification, and steady-state maintenance of tropical cyclones (Emanuel 1986). When deep convection erupts in the eyewall, this gradient in boundary layer θ_e becomes manifest as a gradient in potential temperature θ and temperature T as a result of condensational heating. The diabatic heating (or more precisely, its radial gradient) drives a deep secondary circulation (the radial and vertical flows), with upward motion where there is heating, and compensating subsidence on either side of the heating (Eliassen 1951; Schubert and Hack 1982; Hack and Schubert 1986; Nolan et al. 2007; Pendergrass and Willoughby 2009). This is the generally accepted paradigm, although there are alternative theories regarding the source of the subsidence (Smith 1980). The descent inward of the eyewall is believed to lead to the formation of a nearly cloud-free central region (i.e., the “eye”) and to its further warming relative to the (already warm) eyewall (Shapiro and Willoughby 1982; Vigh and Schubert 2009). Much uncertainty remains about the precise mechanism by which this forced descent occurs, as well as regarding the vertical distribution and magnitude of descent, and its variability in time.

Presumably, the distribution of warming in space and time is determined to a large degree by the distribution of vertical advection of θ . This in turn is related to the distribution of descent and static stability in the eye. However, very few systematic investigations into the time evolution of the eye warming and the relative importance of the various terms that may contribute to such warming have been conducted. Kurihara (1975) performed a temperature budget analysis of an axisymmetric simulation with 20-km horizontal grid spacing and 11 vertical levels. He found that the temperature increase in the “eyewall” was the result of a small positive residual between diabatic heating and adiabatic cooling. Owing to the coarse resolution, the simulation could not resolve an eye. Kurihara and Bender (1982) presented a temperature budget over a 10-min period (during which the storm was intense and near steady-state) for a simulation using a three-dimensional hydrostatic model with parameterized convection (and no explicit microphysics), with 5-km grid spacing and 11 vertical levels. They found that a warming tendency from weak mean descent in the eye was largely balanced by cooling from eddies (primarily horizontal), and that

the effects of diffusion (vertical and horizontal) were small above the boundary layer.

Zhang et al. (2002, hereafter ZLY02) performed a detailed potential temperature budget analysis of a simulation of Hurricane Andrew (1992), at 6-km grid spacing and with 23 vertical levels. The azimuthal mean θ budget was calculated over a 1-h period (using data every 5 min) during which the simulated Andrew was very intense, yet still intensifying. ZLY02 found a narrow zone of diabatic cooling along the eye/eyewall interface, coinciding with the axis of strongest mean descent. Decomposing total advection, ZLY02 found that this zone of diabatic cooling was reinforced by radial advective cooling, and opposed by vertical advective warming, with the total advection yielding a positive tendency in this region. As this net advective warming largely cancelled the diabatic cooling, the actual temperature change over this 1-h period was relatively small and did not resemble the distribution of any one budget term. As compared to advection and diabatic heating, ZLY02 found that the combined contributions of the PBL scheme and subgrid-scale diffusion were relatively small above the boundary layer, and that the radiative tendency was negligible.

While the simulation and budget analysis of ZLY02 yielded many interesting results, there are a few important limitations. One is that 6-km grid spacing is still rather coarse for representing convection and the structure of the eye/eyewall, as is the use of only 23 vertical levels. The other concern is that the budget was only examined over a 1-h period, and it is unclear how representative changes over such a short period are of either longer-period trends or of a hypothetical quasi-steady-state average. For example, the pattern of net temperature change found by ZLY02 consisted of cooling in the eye below 7 km (and in much of the eyewall), and warming in the eye above. ZLY02 concluded that such a pattern is “. . . consistent with the development and strengthening of a warm-cored eye” It is unknown whether or not the temperature change over the whole period of intensification is actually consistent with this picture, and it seems unlikely that a net eyewall cooling would occur. Further, the warming of the eye was said to be due to “slow subsidence warming,” yet ZLY02’s Fig. 3 indicates that radial advection is about the same magnitude but of opposite sign to vertical advection. Ultimately, the above deficiencies render some of the interpretations in ZLY02 questionable. Therefore, much uncertainty remains regarding the pattern and mechanisms of temperature change in the eye of tropical cyclones.

In the control simulation of SN12, the maximum perturbation temperature was found at 5–6-km height

throughout most of the simulation and, as mentioned above, a midlevel maximum was characteristic of a wide range of simulations. Here, we use potential temperature budgets to attempt to understand what leads to such a structure, and why it is different from what conventional wisdom suggests (i.e., an upper-level maximum). Section 2 describes the model setup and basic characteristics of the evolution of a new simulation that we examine. In section 3, we present the budget results for this simulation. In section 4, we synthesize our results and present conclusions.

2. Warm-core structure of simulation

a. Model setup and description of simulation

We use the Weather Research and Forecasting model (WRF), version 3.1.1, to simulate the evolution of an idealized hurricane on a doubly periodic f plane ($f = 5.0 \times 10^{-5} \text{ s}^{-1}$). The SST (28°C), initial vortex profile, and environmental sounding (the moist-tropical sounding of Dunion 2011) are identical to those of the control simulation of SN12, as are the choice of parameterization schemes. Briefly, this includes the Yonsei University (YSU) (Hong et al. 2006) and the WRF single-moment six-class microphysics (WSM6) (Hong and Lim 2006) schemes for parameterization of the planetary boundary layer and of microphysics, respectively, and we use no parameterization of either convection or radiation. We use 40 vertical levels, and a triply-nested grid, with 18-, 6-, and 2-km horizontal grid spacing. The only significant change from SN12 is that here we simulate a hurricane in a quiescent environment, whereas SN12 used a 5 m s^{-1} mean easterly flow. To distinguish the current simulation from the control simulation of SN12, hereafter we refer to the new simulation as NOFLOW. The absence of mean flow is less realistic, but for reasons discussed later, it is necessary for being able to calculate an accurate budget. Nevertheless, the evolution of intensity in NOFLOW is broadly similar to that of the control of SN12 (and nearly identical through 48 h), as shown in Fig. 1. The intensification rate in SN12 slows after 48 h, while in NOFLOW the storm continues rapidly deepening for another 12–18 h. There are two pronounced periods of weakening evident in NOFLOW (72–96 and 120–144 h) that are absent from SN12. However, the maximum 10-m wind speed $V_{\text{max}10}$ achieved is nearly the same in both cases ($\sim 70 \text{ m s}^{-1}$), and differences in $V_{\text{max}10}$ are almost always less than 10 m s^{-1} (Fig. 1b).

b. Evolution of the warm core

We define “the environment” to be the (time evolving) mean temperature averaged in the 550–650-km annulus

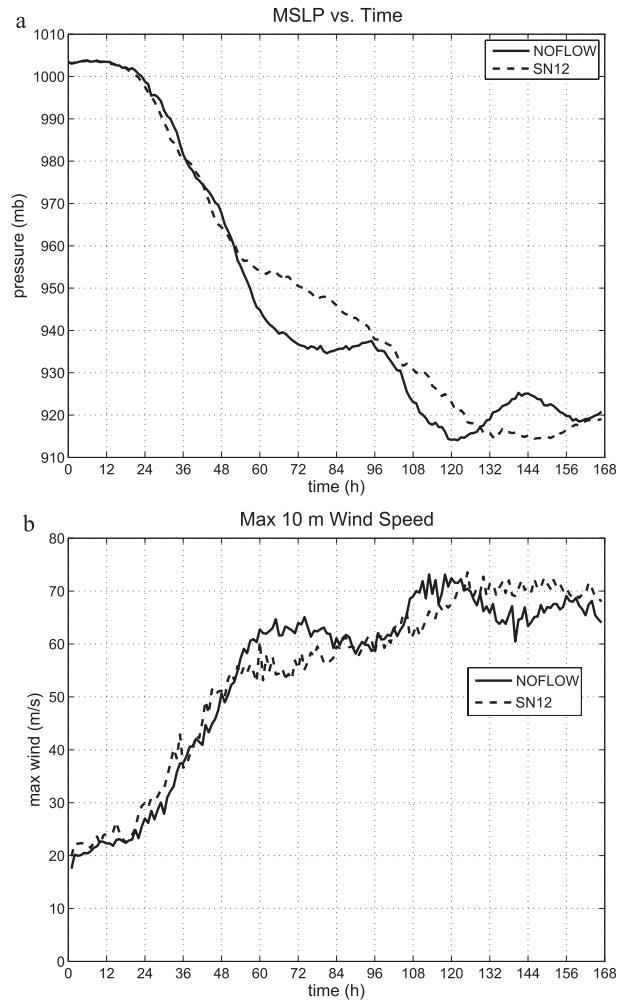


FIG. 1. For NOFLOW and for the control simulation of SN12, time series of (a) minimum sea level pressure, and (b) maximum 10-m wind speed.

(as in SN12). This definition is consistent with those used in recent observational studies (Knaff et al. 2004; Halverson et al. 2006). Figure 2 shows the radius–height structure of perturbation temperature for NOFLOW, every 24 h starting at 0000 UTC day 2 (cf. Fig. 2 of SN12). Starting from an initial condition where perturbation temperature is maximized at about 5.5 km (not shown), the maximum elevates to 7 km after 24 h (whereas in SN12, the maximum elevated to 9 km). This midlevel maximum lowers to 6 km by day 3 and 5 km by day 4 and then rises to 6.5 km on days 5 and 6, and near 8 km by day 7. The general phenomenon of a primary midlevel maximum (4–8 km) in perturbation temperature is consistent with the 15 simulations of SN12. In addition to this primary maximum, two other secondary maxima are seen at times: a low-level maximum near 2 km on day 3, and an upper-level maximum from

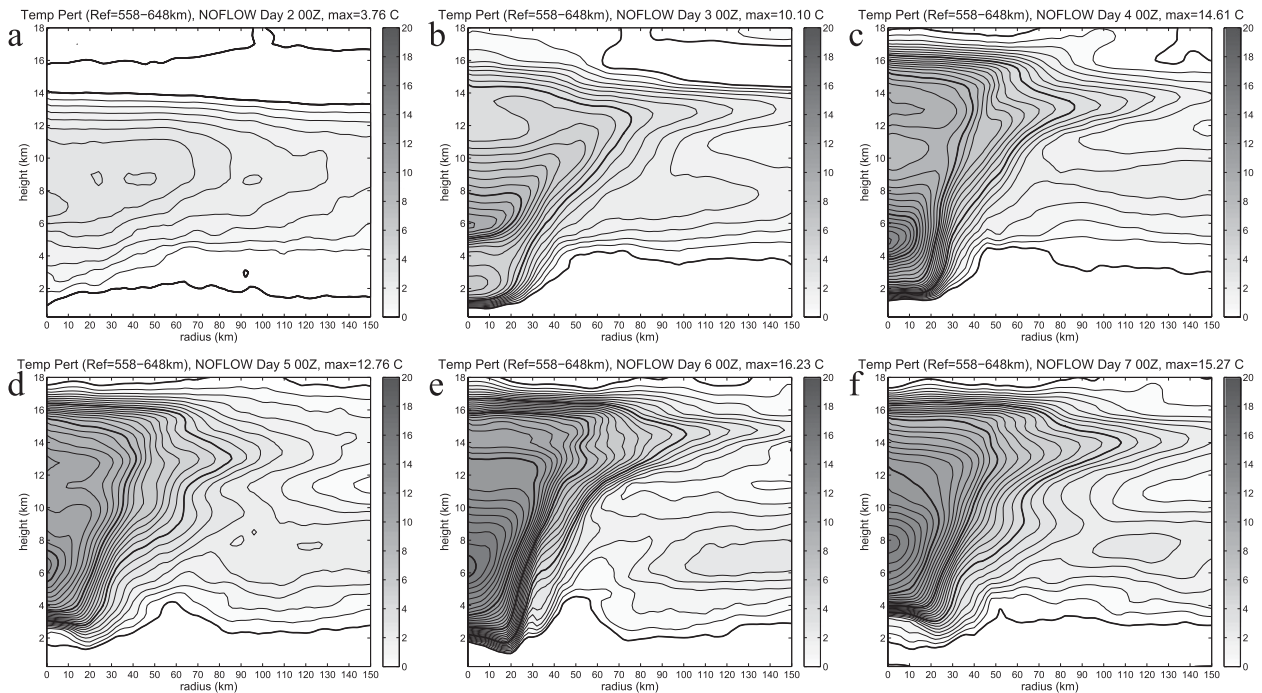


FIG. 2. Perturbation temperature for NOFLOW, every 24 h starting at 0000 UTC day 2. The contour interval is 0.5°C , and the 0° , 4° , 8° , 12° , and 16°C contours are thickened.

12–14 km evident on days 4 and 5. This upper-level maximum was also seen at times in all of the simulations of SN12 but was almost always weaker than the midlevel maximum.

An interesting feature is seen on days 3 and 4, where the perturbation temperature (and therefore the temperature itself) is maximized well away from the center at about 9–12-km height. This phenomenon can also be seen in many of the simulations of SN12 (though not discussed, cf. their Figs. 2 and 4). On day 4, this off-center maximum is associated with the existence of a local minimum (in both radius and height) in perturbation temperature at the storm center in this layer. Inward of the maximum perturbation temperature, the radial temperature gradient is positive, and so through thermal wind balance will be associated with tangential winds increasing with height in this region. This is confirmed in Fig. 3 (also cf. Fig. 1 of SN12), which shows radius–height snapshots of azimuthal-mean tangential wind every 24 h. Inside of 30-km radius, a minimum in tangential wind can be seen near 9-km height on days 3 and 4, with winds increasing upward to a local maximum at 13 km. Later, the tangential wind minimum fades away, consistent with the fact that the temperature becomes maximized at the center. Because of the difficulty in observing the wind and temperature fields in the upper-level eye, it is unknown if these structures

are realistic. However, the temperature structure is reminiscent of the “warm-ring” structure shown by Schubert et al. (2007) to occur at low levels in some tropical cyclones. They attributed the existence of this feature to the descent in the eye being maximized away from the center, which they showed theoretically to occur for storms with large eyes and/or high inertial stability in the eye. An off-center maximum in perturbation temperature at low-levels (1–4 km) is also evident in NOFLOW on and after day 5 (Fig. 2), and there is also a subtle increase of winds with height in the eye at these levels (Fig. 3).

3. Budget analysis

a. Evolution of temperature change and its relationship to perturbation temperature

In this section, we present budgets of θ in order to gain insight into the relevant processes that determine the magnitude and distribution of warming in the eye. While the warm core is generally defined in terms of temperature (as we do here), it is simpler to calculate and interpret a budget of θ since θ is approximately conserved in the absence of diabatic heating. Figure 4 shows consecutive 12-h changes in potential temperature $\Delta\theta$. From an examination of the 12 h changes in temperature ΔT ,

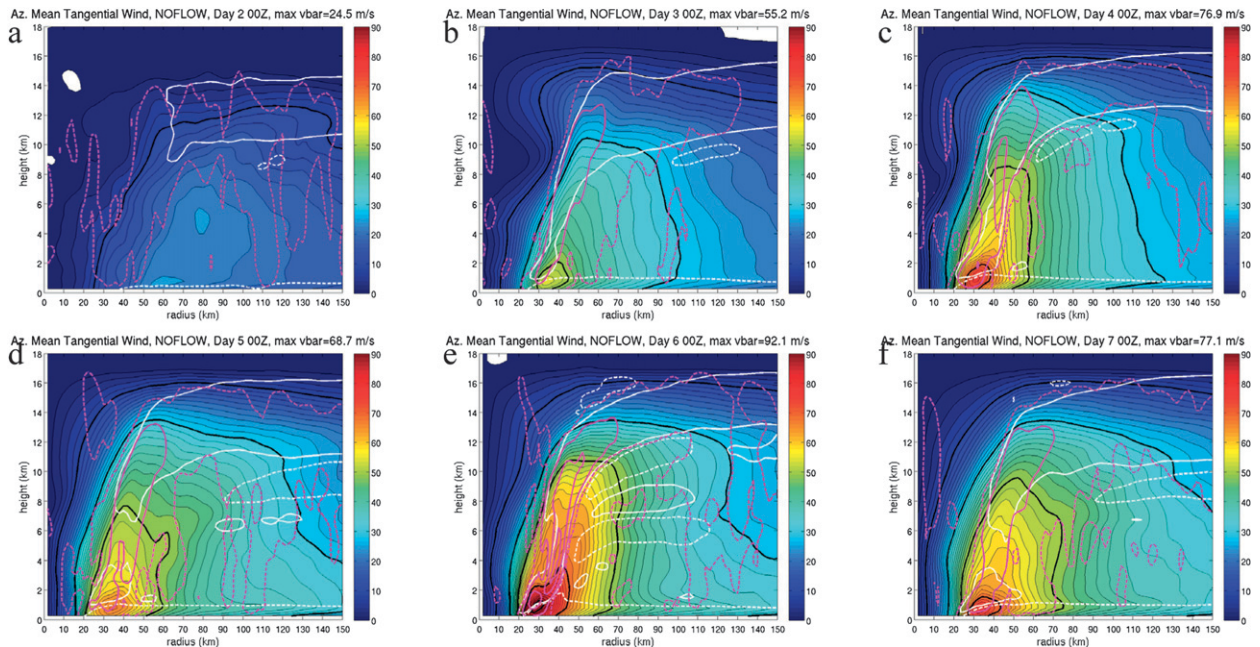


FIG. 3. Azimuthal mean tangential wind (color filled every 2 m s^{-1}), every 24 h starting at 0000 UTC day 2. Contours are thickened every 20 m s^{-1} , starting from 10 m s^{-1} . Radial velocity is contoured in white at $+2$ (solid) and -2 (dashed) m s^{-1} . Vertical velocity is contoured in dashed magenta at $+0.1 \text{ m s}^{-1}$, and in solid magenta at $+1$, $+3$, and $+5 \text{ m s}^{-1}$.

it is clear that the structure of changes in these two variables is qualitatively the same (not shown), and so we can safely use a θ budget to understand the evolution of the warm core as defined by perturbation temperature.

Consistent with thermal wind balance, the greatest warming of the eye occurs during the period of most rapid intensification of the wind field, and periods of weakening exhibit cooling throughout much of the eye. There is large time variability in the spatial structure of $\Delta\theta$, with the maxima and minima being found at different heights for different periods of the simulation. However, this variability does not necessarily manifest as changes in the height of maximum perturbation temperature (i.e., the warm core).

Warming of the entire eye below 15 km occurs from 0000 to 1200 UTC day 2, the start of a 36-h period of rapid intensification (RI).² An absolute maximum occurs at 2-km height, and a secondary maximum is found at 7 km. The low-level maximum in $\Delta\theta$ is not present during the following 12 h, and there is cooling in the

lowest kilometer (more pronounced in ΔT). The maximum $\Delta\theta$ for this period is found at 5.75-km height, and there is a secondary maximum at 14.75 km. Because of the large warming concentrated from 5 to 7 km on day 2, the maximum perturbation temperature becomes established at midlevels (Fig. 2b).³ A secondary maximum in perturbation temperature is seen near 2 km at 0000 UTC day 3 (Fig. 2b), and this is a result of the maximum warming being found there during the first 12 h of day 2. It can also be seen that the off-center maximum in perturbation temperature from 9–12-km height on days 3 and 4 is a result of the region within and just inward of the eyewall (~ 25 – 50 km) warming more rapidly than at the center on day 2.

The final 12 h of RI (0000–1200 UTC day 3) yields the largest θ changes, with a primary maximum at 4.5 km, and a secondary maximum at 14.5 km. Note that in terms of T (not shown) most of the eyewall experiences weak cooling at this time, although θ continues to increase as pressure falls. As a result of the height of maximum warming moving downward slightly, the level of maximum perturbation temperature

² In this budget analysis, we treat the eye as the region inside of the annulus of deep convection, which we (arbitrarily) define by the 10 cm s^{-1} azimuthal mean updraft. We note that by some definitions of the eye (Vigh et al. 2012), an eye does not form in our simulation until the beginning of day 2.

³ Note that, although the perturbation temperature is maximized at 5.5 km in the initial condition (not shown), this does not actually have any noticeable effect on the long-term evolution, as shown in Stern (2010).

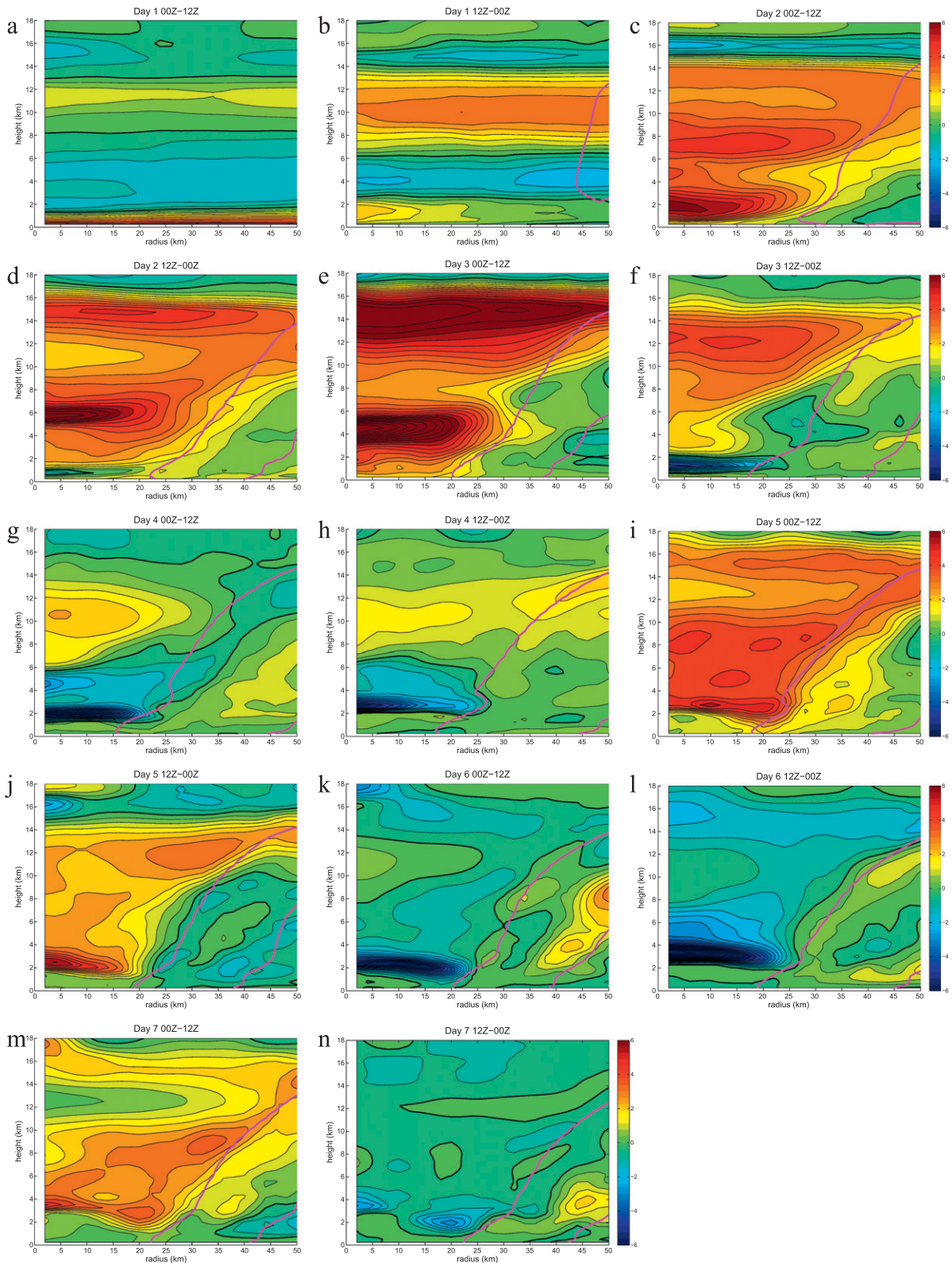


FIG. 4. Twelve-hour changes in azimuthal mean θ , for consecutive 12-h periods beginning 0000–1200 UTC day 1. Contours are every 0.5°C from -10.0° to $+10.0^\circ\text{C}$ (color bar from -6.0° to $+6.0^\circ\text{C}$), with the zero contour thickened. The 12-h-mean $+0.10\text{ m s}^{-1}$ azimuthal mean vertical velocity is contoured in magenta. Note that the radial scale has been restricted to the inner 50 km, so as to focus on the eye.

moves down to 5 km by 1200 UTC day 3, and the distinct low-level maximum is eliminated. From an examination of ΔT over shorter time intervals (not shown), it is clear that the height of the primary maximum in warming lowers quasi-continuously during RI. The continued existence of a secondary upper-level maximum in $\Delta\theta$ leads to the formation of a secondary maximum in perturbation temperature near 14 km at 1200 UTC day 3.

For the next three 12-h periods (1200 UTC day 3–0000 UTC day 5), the absolute maximum $\Delta\theta$ occurs at upper-levels (10–12.5 km), there is no midlevel maximum, and for the latter 24 h there is actually cooling near the height of maximum perturbation temperature (and the intensity weakens). Despite this, the warm-core maximum remains at midlevels (although it does move upward to 6.5 km by 0000 UTC day 5). In fact, it is the upper-level warm-core maximum that becomes less distinct by the end of this period, as the warming is strongest near the region (9–12 km) where perturbation temperature was previously a minimum. Very strong cooling occurs in the lower to midtroposphere within the eye, with the level of strongest cooling rising upward from 1.25 to 2.75 km during this 36-h period. There is a corresponding rise of the level of maximum static stability (not shown), which is indicative of sustained mean ascent within the low-level eye, and the base of the temperature inversion rises from 500 m to 2.5 km (not shown). This low-level cooling is reversed on day 5 during a period of renewed intensification, and warming occurs throughout much of the eye, maximized at 2.5–3.0 km. Despite a maximum in warming well below the height of the maximum in perturbation temperature, the height of the maximum warm core does not change, as its amplitude is now quite large ($>16^{\circ}\text{C}$).

A second period of weakening occurs on day 6, and this is also associated with very large cooling [as much as -9°C ($12\text{ h})^{-1}$] at low- and midlevels, strongest between 2- and 3.5-km heights. Substantial cooling is present up to 7-km height, and as a result, the height of the maximum perturbation temperature rises to near 8 km (where $\Delta\theta$ is near zero) by 0000 UTC day 7. In a reversal from the previous day, there is weak warming in the lowest 1 or 2 km of the eye. Finally, on day 7 there is slight intensification of the storm followed by a near steady state, and this corresponds with a period (0000–1200 UTC) of warming throughout the eye (maximized at 3.5 km), followed by a period (1200–0000 UTC) of near-zero $\Delta\theta$ in much of the eye. As $\Delta\theta$ is larger below than at 8 km, the height of maximum perturbation temperature moves downward again on day 7 (not shown).

b. A potential temperature budget

We now investigate the mechanisms by which the changes in T and θ described in the previous subsection occur. This is accomplished by calculating a budget of azimuthal mean θ , based on the following equation:

$$\Delta\theta = (\text{TADV} + \text{HEAT} + \text{PBL} + \text{HDIF})\Delta t. \quad (3.1)$$

$\Delta\theta$ is the actual change in potential temperature over a given period ($\Delta t = 12\text{ h}$, except where made explicit otherwise). TADV is the tendency on azimuthal mean θ from the total advection (horizontal plus vertical). HEAT is the tendency from azimuthal mean diabatic heating. PBL is the tendency from the boundary layer parameterization scheme, which in addition to tendencies within the boundary layer itself, yields tendencies from subgrid-scale vertical diffusion throughout the free atmosphere. HDIF is the tendency from subgrid-scale horizontal diffusion and also includes the effects of sixth-order numerical diffusion, as well as Rayleigh damping above 16 km.⁴ At each available time, each of the four terms on the RHS of (3.1) is taken directly from model output, and then azimuthally averaged following the procedure described in Stern and Nolan (2011). These tendencies (K s^{-1}) are averaged over the time period corresponding to $\Delta\theta$ and then are multiplied by the length of the period to yield equivalent units (for most cases presented, in kelvins per 12 h).

As far as we are aware, no previous study of a tropical cyclone temperature or potential temperature budget has shown the accuracy of their calculations. There are a number of different pathways that may introduce errors into such budgets, including interpolation from model surfaces to a regular grid, missing terms, sampling frequency, and the effect of storm motion.^{5,6} This latter

⁴ We use standard second-order horizontal diffusion on model coordinate surfaces (“diff_opt=1” in WRF). The eddy viscosity is the standard first-order Smagorinsky scheme, based on the deformation and a mixing length (which is proportional to grid-spacing; “km_opt=4” in WRF).

⁵ In WRF, it is only possible to output the advective tendency after the “big” advective time steps. There are acoustic steps after each of the 3 big substeps of the RK3 integration. We output the tendency after the last of these big steps, which necessarily neglects any changes that occur in the final set of acoustic steps. This error is believed to be small.

⁶ When the storm center moves, the set of gridpoints at which terms are evaluated changes, and so there is a change in mean θ at these times that is not given by any of the forcing terms. Ideally, it should be possible to account for this by calculating the storm-relative advection. However, this is not easily done within a simulation, and interpolation errors were too large when attempting to do this outside the model.

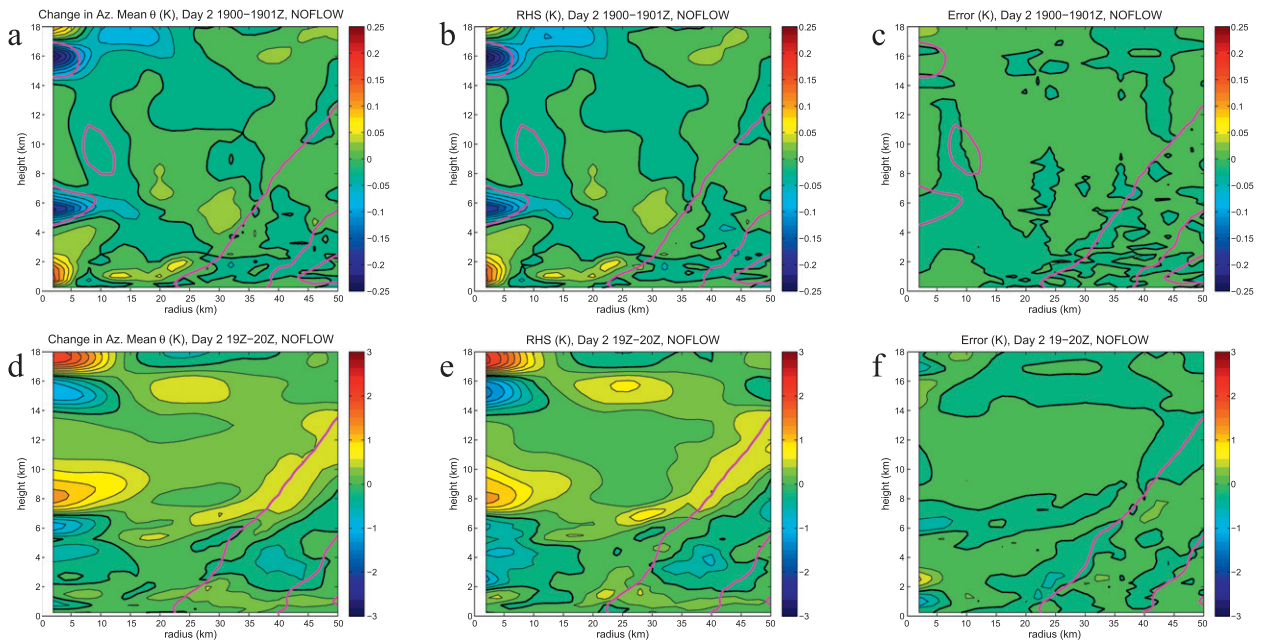


FIG. 5. (a),(d) The change in θ ($\Delta\theta$), (b),(e) the sum of the right-hand-side of (3.1) (RHS), and (c),(f) the difference between $\Delta\theta$ and RHS (error). These are shown for periods of (a)–(c) 1 min and (d)–(f) 1 h. Note that the range and contour intervals are different in each row. The contour intervals are 0.025 and 0.1 K for the top and bottom rows, respectively. The period-averaged azimuthal mean contour of $+0.1 \text{ m s}^{-1}$ vertical velocity is in magenta.

effect can be surprisingly large and is the reason that we examine the NOFLOW simulation in this study, instead of the control simulation of SN12.⁷ Figure 5 shows $\Delta\theta$, the sum of the RHS of (3.1), and the difference between them (i.e., the error) for periods of 1 min and 1 h, within the RI phase of the simulation, using data output at 1-min intervals. The error is quite small for the 1-min period, and in most of the regions with substantial $\Delta\theta$, it is only a few percent. Over the 1-h period, the errors are somewhat larger, but qualitatively, RHS and $\Delta\theta$ agree rather well. We chose this period to illustrate that there can be significant transient fluctuations in $\Delta\theta$ on hourly time scales that are not representative of the long-term evolution of the storm. In this case, there is a deep layer of cooling from 2- to 7-km heights inside of 15-km radius, and this occurs within the RI phase. From looking at $\Delta\theta$ over the 12-h period (Fig. 4d), it can be seen that this 1-h cooling is unrepresentative. This raises doubts about the robustness of the budget analysis and interpretation of ZLY02, who only examined a single 1-h period.

Figure 6 shows the errors for five different 12-h periods (described further below) using 6-min data. The errors tend to increase as the period over which the budget is assessed increases, and for some periods, the errors can be quite large. However, the largest errors are in the regions of large gradient, not the locations of the maxima. It is clear that the magnitudes and spatial organizations of RHS and $\Delta\theta$ agree well qualitatively, and so our budget calculations are sufficiently accurate for purposes of determining the relative importance of the various terms which contribute to the warming of the eye.

Figure 7 shows the four terms that sum to the RHS of (3.1) (using 6-min data), for the three consecutive 12-h time periods from 0000 UTC day 2 to 1200 UTC day 3 (during RI), the period from 0000 to 1200 UTC day 4 (a period of near-steady-state intensity), and the period from 0000 to 1200 UTC day 6 (during weakening).⁸ Each plot is contoured from -6.0 to $+6.0 \text{ K (12 h)}^{-1}$, with the same color bar as for $\Delta\theta$ in Fig. 4. The magnitudes of diabatic heating and advection greatly exceed this range in the eyewall [e.g., almost $1000 \text{ K (12 h)}^{-1}$ on day 6].

⁷ The storm in SN12 moves steadily westward. As expected, the storm in NOFLOW does not move much, but it does drift from its initial location by about 20–40 km throughout the 7-day simulation, and moves 50 km southward during the final 18 h (not shown).

⁸ For this simulation, we have carefully compared budgets computed with different output frequencies and found that 12-h budgets from 6-min output were very similar to those from 1-min output.

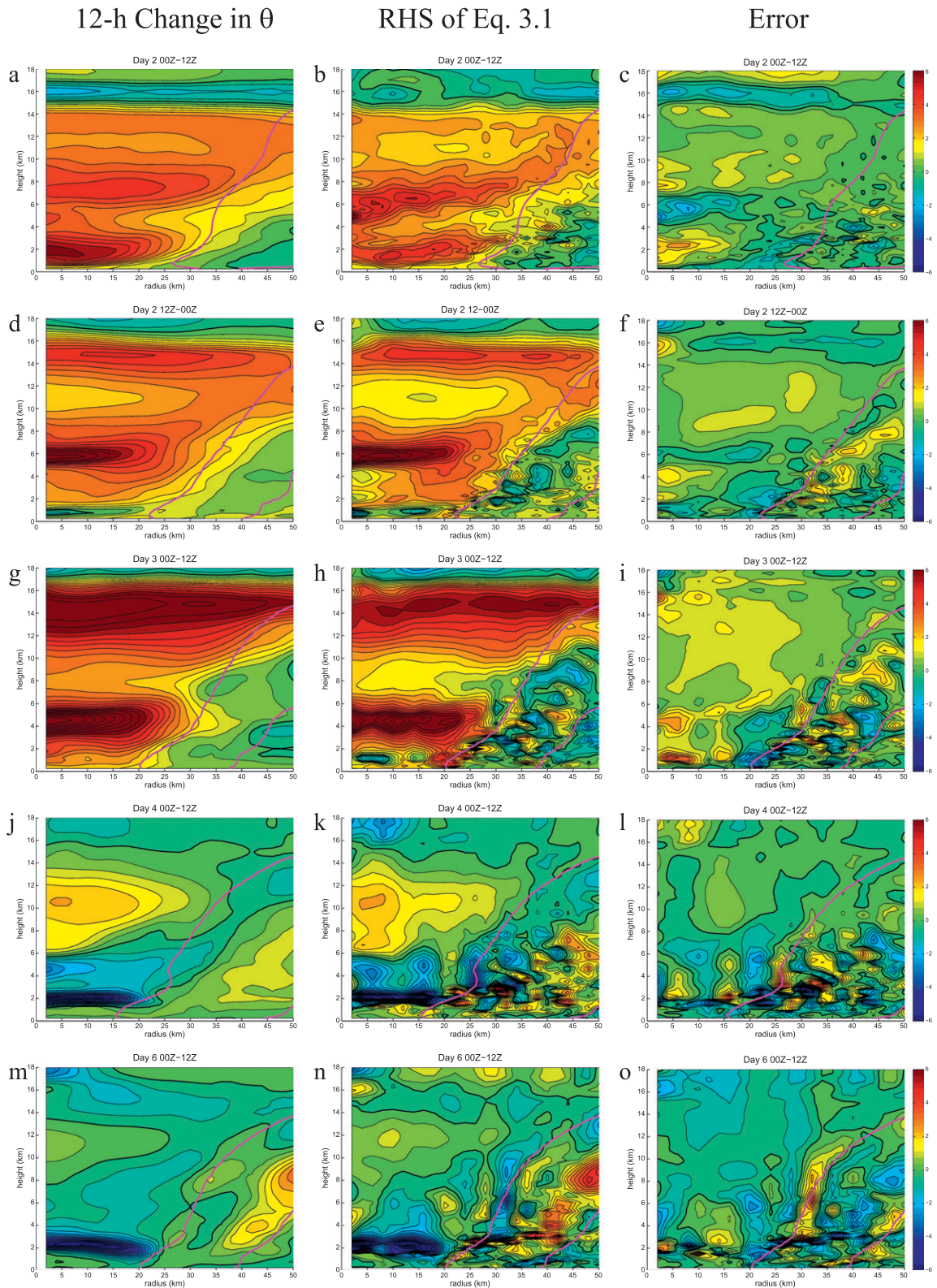


FIG. 6. As in Fig. 5, but for five different 12-h periods, using 6-min data. This is shown for (top to bottom) 0000–1200 UTC day 2, 1200–0000 UTC day 2, 0000–1200 UTC day 3, 0000–1200 UTC day 4, and 0000–1200 UTC day 6. Each field is contoured from -10.0 to $+10.0$ K (color bar from -6.0 to $+6.0$ K), every 0.5 K. The zero contour is thickened, and in each panel, the $+0.10$ m s⁻¹ contour of (time averaged) azimuthal mean vertical velocity is in magenta.

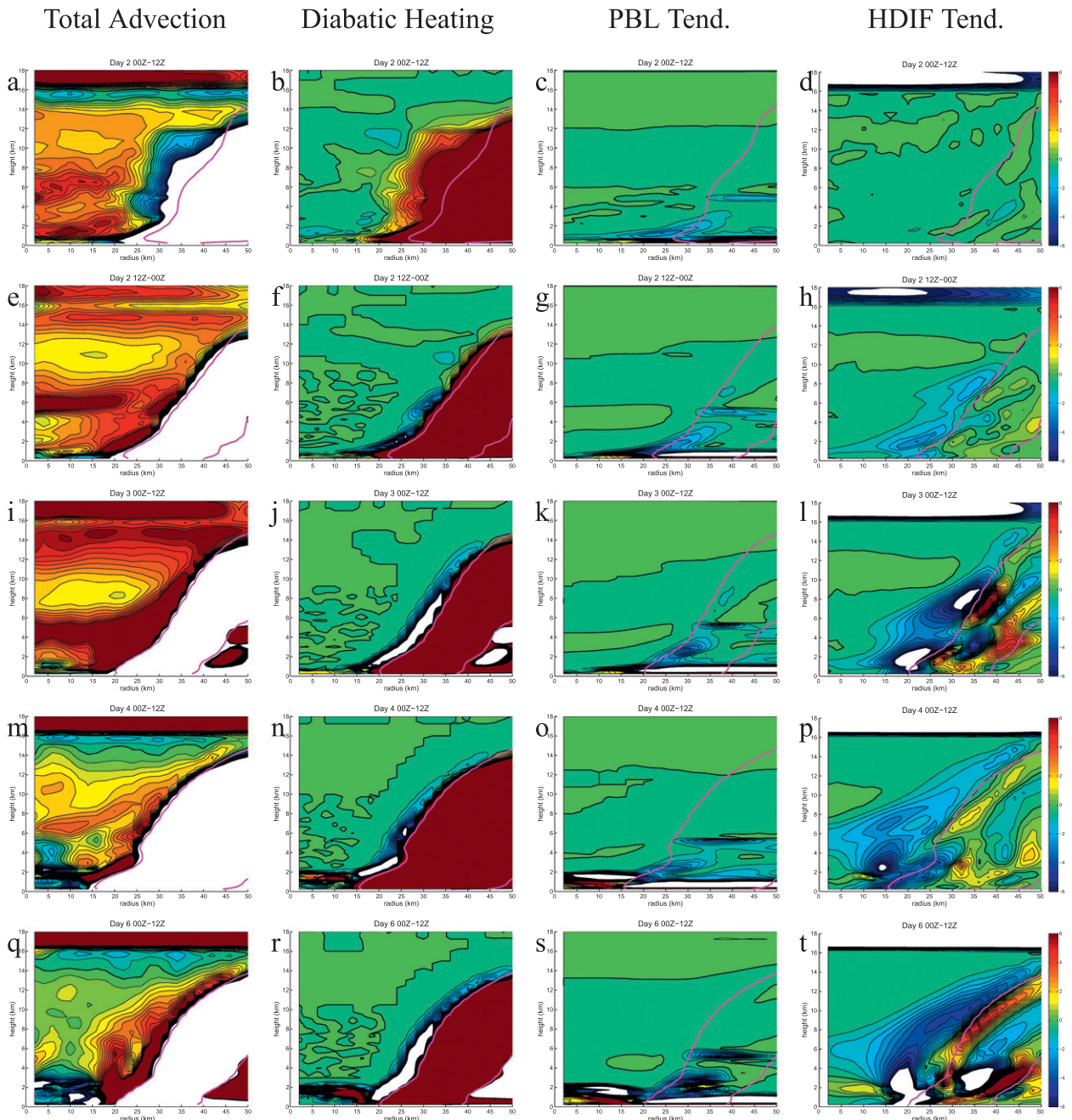


FIG. 7. (left to right) The tendency on azimuthal mean θ from total advection (TADV), diabatic heating (HEAT), the PBL scheme including vertical diffusion (PBL), and horizontal diffusion including Rayleigh damping (HDIF). This is shown for (top to bottom) 0000–1200 UTC day 2, 1200–0000 UTC day 2, 0000–1200 UTC day 3, 0000–1200 UTC day 4, and 0000–1200 UTC day 6. Each field is contoured from -6.0 to $+6.0$ $\text{K} (12 \text{ h})^{-1}$, every $0.5 \text{ K} (12 \text{ h})^{-1}$. The zero contour is thickened, and in each panel, the $+0.10 \text{ m s}^{-1}$ contour of (time averaged) azimuthal mean vertical velocity is in magenta.

These two terms largely cancel each other in regions of significant diabatic heating, and we wish to focus on the much smaller tendencies that occur within the eye. Looking first at 0000–1200 UTC day 2 (Figs. 7a–d), it can be seen that inside of the region of substantial diabatic heating, TADV is the only significant term, and so it is

clear (cf. Fig. 4c) that the magnitude and spatial distribution of warming in the nascent eye is largely due to advection. PBL is large in a thin layer near the surface, and cooling tendencies as large as $-0.5 \text{ K} (12 \text{ h})^{-1}$ extend upward to 3 km near the eye/eyewall interface. At this time, HDIF is negligibly small, except in the

Rayleigh damping layer (>16-km height). In the subsequent 12-h period (Figs. 7e–h), TADV exhibits a maximum at about 6 km, with a tendency of greater than 6 K (12 h)^{-1} inside of 20-km radius. There is a secondary maximum near 14.5-km height that extends radially throughout the eye. Note that between 10- and 12-km heights, TADV is maximized well away from the center (25–40-km radius). All of these features are quite similar to those seen in $\Delta\theta$ (Fig. 4d), and so total advection of potential temperature can largely explain the distribution of warming throughout most of the eye during this period.

Just inward of the eyewall, there are narrow local maxima in TADV at low and midlevels. These tendencies do not manifest as similar changes in θ , as $\Delta\theta$ decreases monotonically with increasing radius here. It can be seen that there are similarly shaped regions of diabatic cooling along the eye/eyewall interface that largely cancel the advective tendencies (consistent with ZLY02). The effects of horizontal diffusion, while still relatively small, have increased substantially from the first 12-h period, with a broad region of less than $-0.5 \text{ K (12 h)}^{-1}$ in a 15-km-wide zone just inward of the eyewall. The strongest diffusive cooling tends to be nearly collocated with local maxima in advective warming. So, while advection is the only important term contributing to $\Delta\theta$ in the region near the center of the eye, as the intensity of the storm increases, other terms become significant in the outer portion of the eye.

During the final 12-h period of RI (0000–1200 UTC day 3), the features seen on the latter half of day 2 become further accentuated (Figs. 7i–l). The height of the midlevel maximum in TADV lowers somewhat, consistent with the change in $\Delta\theta$, and TADV increases with height from a minimum at 8 km to a secondary maximum near 14 km, also consistent with $\Delta\theta$. A narrow (~ 5 km wide) zone of intense diabatic cooling lies just inward of the sloping eyewall throughout the free troposphere. As in the previous period, this cooling cancels much of the advective warming in this region. HDIF has now become rather large in a 10–15-km-wide region inward of the eyewall, with local extrema from near the surface to 2.5 km and from 7- to 9-km heights. That HDIF can be of the same magnitude as HEAT and TADV is somewhat in contrast to ZLY02, although their Fig. 2 indicates that the maximum diffusive cooling in their simulated Andrew was as large as 25% of the maximum diabatic cooling.⁹

The period from 0000 to 1200 UTC day 4 is one of near-zero change in terms of minimum sea level pressure (MSLP) and slight weakening in terms of $V_{\text{max}10}$ (Fig. 1). As seen in Fig. 4g, the structure of $\Delta\theta$ in the eye at this time is characterized by slight warming from the surface to 1 km, strong cooling near 2 km, weaker cooling extending to 6 km, and moderate warming from 6 to 16 km, maximized near 10.5 km. Unlike in the three previous periods examined, this structure is not really reflected by the TADV field (Figs. 7m–p), at least below 8-km height. This is because the cooling from HDIF is now substantial throughout most of the low- and midlevel eye. In particular, the maximum in TADV near 6.5 km is largely cancelled by HDIF, leading to the maximum in $\Delta\theta$ being near 10.5 km. As TADV in the center of the eye is substantially smaller than during RI, the absolute maximum in TADV is now along the edge of the eyewall at nearly all heights. Again, however, this does not lead to maxima in the $\Delta\theta$ field (and there is actually net cooling in much of this region), due to diabatic cooling and (to a lesser extent) HDIF. The cooling in the midlevel eye appears to be due to a combination of TADV and HDIF, and the strong cooling near 2 km has contributions from TADV, HDIF, and PBL, which is now large and negative from 1- to 2-km height. A thin layer of diabatic heating in the eye from 1 to 2 km partially offsets the cooling. The weak warming of the lowest kilometer is due to PBL, which outweighs the cooling from the other terms in this layer.

In many ways, the structure of the different terms of (3.1) on 0000–1200 UTC day 6 (Fig. 7, fifth row) is similar to that two days earlier. The storm is at peak intensity at the beginning of this period but undergoes a relatively large weakening during these 12 h. There is very large cooling from 2- to 4-km height inside the eye (Fig. 4k), owing to a combination of TADV and PBL. Weaker cooling from 4 to 8 km near the center and extending throughout the troposphere in the outer portion of the eye is due entirely to HDIF. TADV is actually positive throughout the eye from 4- to 14-km height, and it is the substantial cooling from HDIF that renders the net θ tendency negative everywhere except for a relatively small area near the center from 8- to 13-km height, a region where HDIF is small. Once again, there is strong advective warming at the eye/eyewall interface that is cancelled by equally strong diabatic cooling. That this occurs during a period of substantial weakening indicates that the existence and strength of these features is related to the intensity of the storm and not to the intensity trend. A zone of moderate advective warming extends inward from 25- to 15-km radius within the eye, and this is entirely cancelled by HDIF. It is clear that for this simulation, horizontal diffusion plays an

⁹ While ZLY02 do not make clear what precisely is included in their “PBL and diffusion” term, it appears that it includes both vertical and horizontal diffusion, and that horizontal diffusion is the main contributor to this term above the boundary layer.

important role in the maintenance of temperature within the eye, once the storm is sufficiently intense.

c. Decomposing advection into horizontal and vertical, mean and eddy

As presented in the previous subsection, TADV represents the contribution to $\Delta\theta$ from the total advection. It would be useful to separately output the tendencies from horizontal and vertical advection. Unfortunately, this cannot be easily done within WRF, because the individual terms are calculated in flux form, and so while their sum is equal to total advection, individually the fluxes do not correspond to their respective advectives. To examine the horizontal and vertical advective tendencies, we must calculate them offline from the radial (u) and vertical (w) wind fields and from the θ field, after we have calculated azimuthal means and interpolated these fields onto a regular radius–height grid. This introduces additional errors, which are not always negligible, especially in regions of large gradients. Within the eye, however, the sum of the interpolated terms is qualitatively the same as TADV from the direct model output (not shown), and so we can use them to gain further insight into the budget. In addition to separating advection into its horizontal and vertical components, we further split each of these terms into a mean and eddy tendency. For example, the tendencies on azimuthal mean θ from azimuthal mean radial and vertical advection are $\text{RADVM} = -\bar{u}(\partial/\partial r)\bar{\theta}$ and $\text{VADVM} = -\bar{w}(\partial/\partial z)\bar{\theta}$, respectively. The tendencies on azimuthal mean θ from the eddy advectives can be written in terms of the divergences of eddy fluxes (flux form), given by $\text{RADVE} = -(\partial/\partial r)(\overline{u'\theta'}) - (\overline{u'\theta'}/r)$ and $\text{VADVE} = -(\partial/\partial z)(\overline{w'\theta'})$. In the above definitions, the overbars denote the azimuthal mean, and the primes denote the deviation from the azimuthal mean. Figure 8 shows these four terms for the same respective periods as shown in Fig. 7.

A few common characteristics can be seen at all times for these advection terms. First, well inside the eye, RADVM is always small, as both the mean radial θ gradient and mean u go to zero as the center is approached. Second, once a sufficient intensity is reached, a narrow zone of radial advective cooling develops along the eye/eyewall interface. This inflow axis is coincident with the axis of maximum descent and diabatic cooling, consistent with the results of ZLY02.

VADVM is often the largest component of TADV inside the eye, as expected. However, it is not always the largest component at the location of maximum $\Delta\theta$. In fact, during 0000–1200 UTC day 2 (Figs. 8a–d), VADVM is actually negative (cooling tendency) throughout the eye from 6- to 8.5-km height. Since θ increases with

height, this means that there is actually mean ascent over a 12-h period in the midlevel eye (Fig. 9a, further discussed in section 3e), during RI. Further, as net warming (and TADV) is a positive maximum in this region, some process other than mean vertical advection must be responsible for the largest warming during this period. It can be seen that this process is eddy radial advection (RADVE).

In the same region where VADVM is negative, RADVE is a positive maximum. In the following 12-h period (1200–0000 UTC day 2, second row), RADVE is also large and maximized near 6 km (the height of maximum $\Delta\theta$), and VADVM is near zero from 6–8 km. In general, the regions of significant RADVE in the eye are collocated with opposite-signed regions of significant VADVM. Note that the midlevel TADV maximum during intensification is not always due to RADVE: during the 12-h period of greatest warming (0000–1200 UTC day 3, Figs. 8i–l), VADVM is maximized at the height of greatest $\Delta\theta$, while RADVE is relatively small there. During this period, it is also evident that the local minimum in TADV (and $\Delta\theta$) near 8 km is a result of VADVM being minimized near this height.

d. Why is RADVE positive in the eye during intensification?

One of the more interesting characteristics of the budget is that RADVE can be quite substantial well inside the eye, and that this term appears to be responsible for most of the midlevel warming during the first 24 h of RI. This is contrary to our expectation (and to results from previous studies) that mean vertical advection would always be the dominant mechanism of warming. Further, it is somewhat puzzling that the asymmetries can lead to a warming tendency at all, given that the mean radial gradient of θ is negative. We address this conundrum of apparent up-gradient mixing by carefully examining the θ and u fields, their asymmetries, and the relationship between them. Figure 10a shows a storm-centered horizontal cross-section of θ at 6.3-km height (near where both $\Delta\theta$ and RADVE are maximized) at 1800 UTC day 2.¹⁰ While the azimuthal mean θ is maximized at the center at this height (not shown), the total θ is not, and instead it is found 15 km SSW of the center. The asymmetric components of potential temperature θ' and radial velocity u' are shown in Figs. 10b and 10c, respectively. Both fields are dominated by a coherent wavenumber-1 structure, with

¹⁰ These quasi-horizontal cross sections are actually along model half-levels, and 6.3 km is the mean height of level 23.

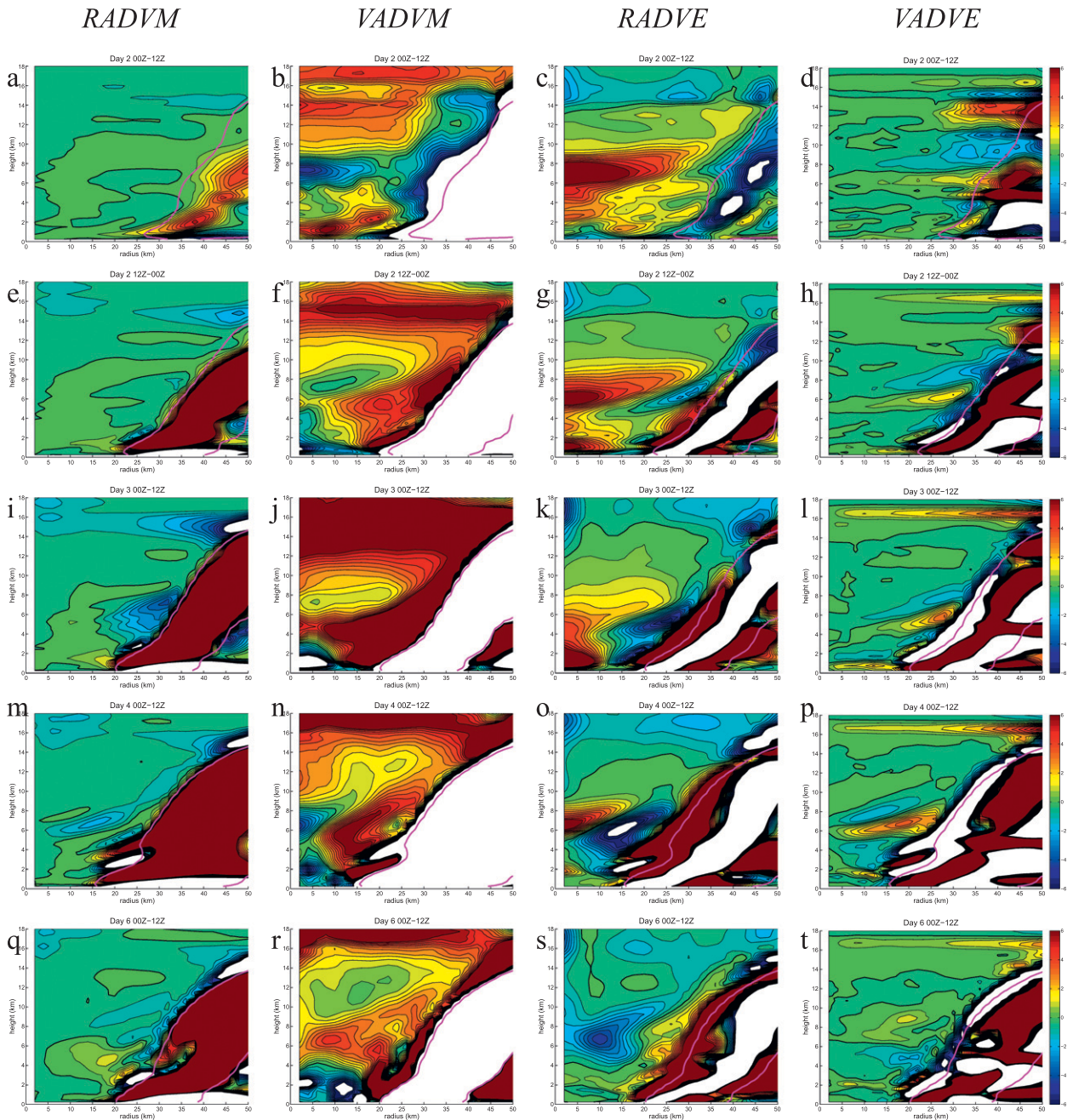


FIG. 8. As in Fig. 7, but (left to right) the tendency on azimuthal mean θ from azimuthal mean radial advection (RADVM), azimuthal mean vertical advection (VADVM), eddy radial advection (RADVE), and eddy vertical advection (VADVE). Each field is contoured from -6.0 to $+6.0 \text{ K (12 h)}^{-1}$, every $0.5 \text{ K (12 h)}^{-1}$. The zero contour is thickened, and in each panel, the $+0.10 \text{ m s}^{-1}$ contour of (time averaged) azimuthal mean vertical velocity is in magenta.

warmer air and inflow to the SSW, and colder air and outflow to the NNE. Because the θ' and u' fields are nearly 180° out of phase with each other, the sign of the eddy flux is the same (negative) on both sides of this couplet (Fig. 10d), and the magnitude of the divergence of its azimuthal mean is substantial, yielding a warming

tendency inward of the location where the perturbations are maximized ($\sim 25\text{-km}$ radius).

An examination of animations of these fields (not shown) indicates that while the above-described structure is not continuously present, it occurs for periods of 1–3 h at a time, and this pattern recurs several times over

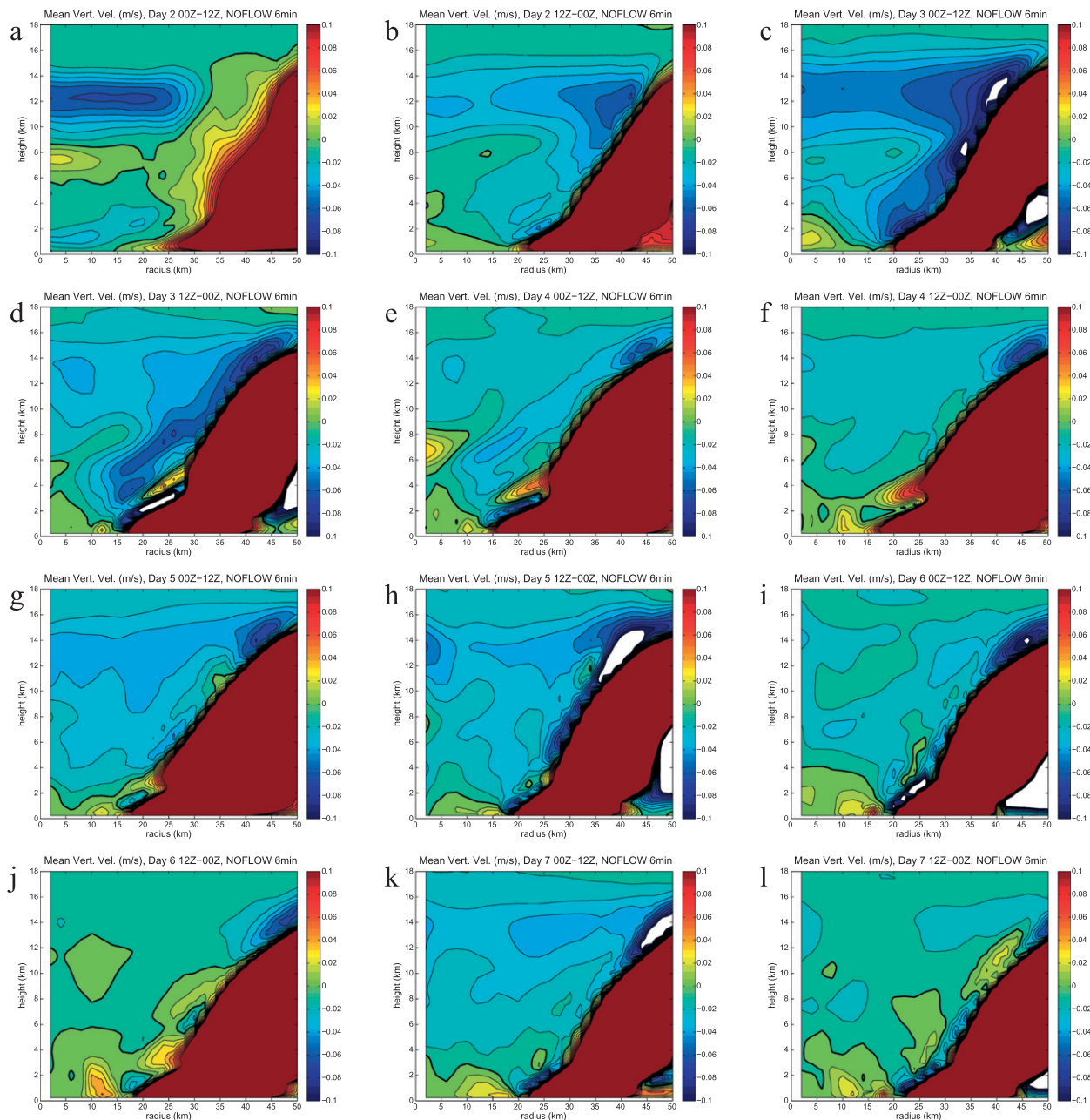


FIG. 9. Azimuthal mean vertical velocity, averaged over consecutive 12-h periods from 6-min data, beginning at 0000 UTC day 2. Contouring is from -0.1 to $+0.1$ m s^{-1} , every 0.01 m s^{-1} . The zero contour is thickened.

a 12-h period, with the result being that net warming is accomplished by this mechanism. As this simulation is performed in a homogeneous and quiescent environment on an f plane, there is no environmental mechanism for forcing such a wavenumber-1 asymmetry. Accordingly, the peaks in the asymmetric fields rotate with time, with an apparent period of roughly 2–3 h. The most plausible source of this asymmetry is the excitement of a wavenumber-1 instability. Nolan

et al. (2001) showed that the wavenumber-1 instability, which exists for any vortex where the angular velocity is maximized away from the center, represents a displacement of the low-vorticity core of a vortex within the larger-scale circulation. This is responsible for the often-observed trochoidal oscillation (“wobble”) of the pressure minimum, and is an important mechanism for mixing between the eye and the eyewall. We believe that the asymmetric mixing and

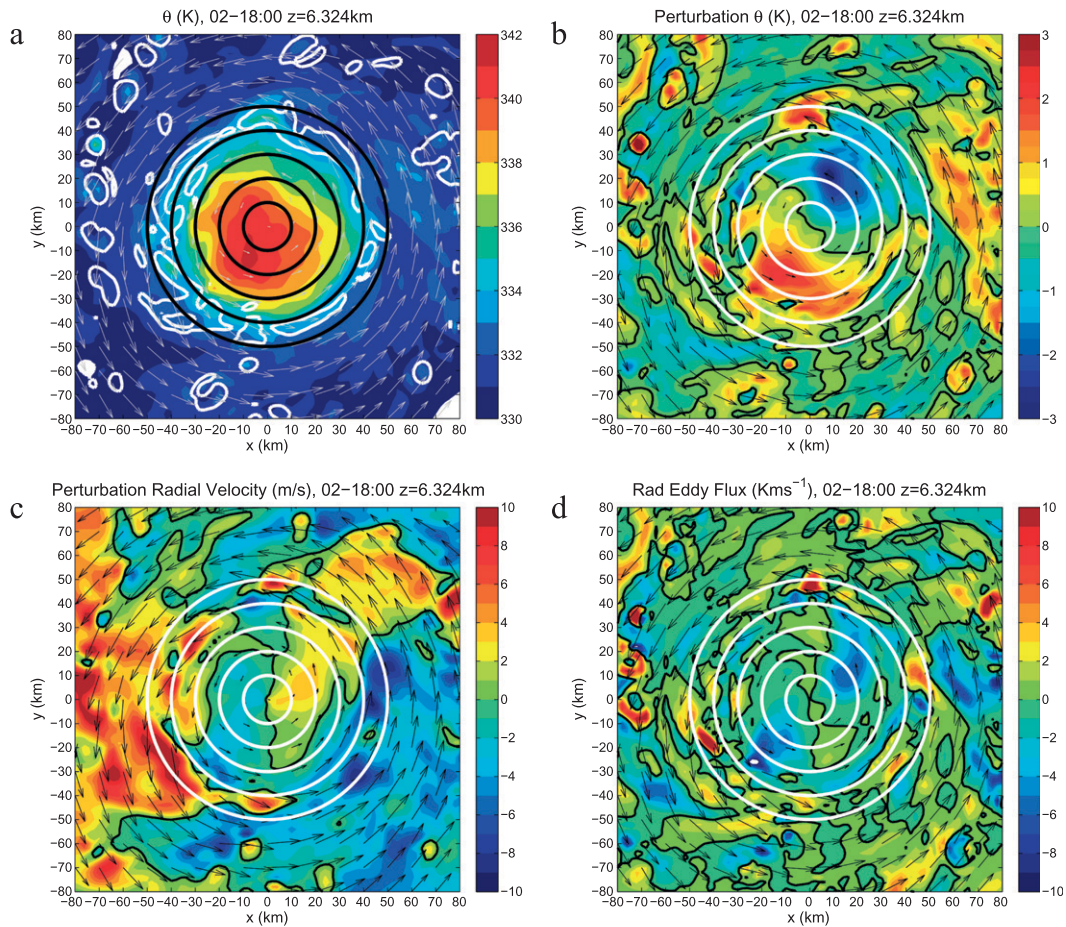


FIG. 10. At 1800 UTC day 2, horizontal cross sections at about 6.3-km height of (a) θ , (b) the asymmetric component of θ , (c) the asymmetric component of u , and (d) the radial eddy flux of θ . In (a), θ is contoured every 1 K, and the 1 m s^{-1} updraft contour is in white. In (b), asymmetric θ is contoured every 0.25 K from -3.0 to $+3.0$ K. In (c), asymmetric u is contoured every 1 m s^{-1} . In (d) the eddy flux is contoured every 1 K m s^{-1} . In each plot, horizontal wind vectors are shown every 5 grid points, and range rings are drawn every 10 km.

warming we see here is likely a manifestation of this instability.

e. Structure of mean vertical velocity in the eye

To further aid in our understanding of the budget, we briefly examine the structure and evolution of time- and azimuthal-mean vertical velocity in the eye (Fig. 9). Several important characteristics of the eye descent are made clear. First, mean descent well inside the eye is generally quite small (compared to the instantaneous local values; not shown), at most $5\text{--}6 \text{ cm s}^{-1}$ during the beginning of RI, and $1\text{--}3 \text{ cm s}^{-1}$ at most other times. Next, although during the first 12 h of RI, the region of maximum descent is radially broad and extends to the center, once a sufficient intensity is reached, descent becomes concentrated just inward of the eyewall, in agreement with Liu et al. (1999) and consistent with our

budget analysis (as well as the theory of Schubert et al. 2007). At times, this mean descent can be as large as $10\text{--}20 \text{ cm s}^{-1}$, and it tends to have two maxima, near 14- and near 2-km height. Near the center of the eye, descent tends to be maximized near 12–13 km during periods of intensification. During periods of weakening or near steady state, there is less structure in the vertical velocity field. Finally, at all times after 0000 UTC day 2, there is mean ascent throughout the low-level eye, generally encompassing the lowest 2–3 km, and in some periods this layer extends as high as 4–6 km. Comparing to Fig. 4, it is clear that the large fluctuations in θ between 2 and 4 km are associated with day-to-day reversals in the sign of mean vertical velocity in this layer. In the second part of this study (Stern and Zhang 2012, manuscript submitted to *J. Atmos. Sci.*, hereafter Part II), we will examine both the mean and instantaneous

vertical velocity fields in greater detail, through trajectory analyses.

4. Discussion and conclusions

In this study, we investigated the structure of the warm core in tropical cyclones, through a detailed potential temperature budget analysis of a simulation conducted in a quiescent environment. SN12 showed that across a wide range of simulations, the maximum perturbation temperature consistently was found at midlevels (4–8-km height), at all times. Here, we showed that this is because the very large warming that occurs during the initial rapid intensification is maximized at midlevels. During periods of slower intensification, quasi-steady state, or weakening, the maximum in warming ΔT is often found at upper levels (10–12 km), while the maximum perturbation temperature remains at midlevels.

During RI, there is a secondary upper-level maximum in ΔT near 12–14-km height, leading to the formation of a similar relative maximum in perturbation temperature. The entire eye between 2- and 15-km height warms during periods of intensification. In contrast, during periods of weakening, while cooling generally occurs in the lower 6 km of the eye, much of the upper-level eye continues to warm, leading to an increase in height of the maximum warm core. Another region where large ΔT is often found is near the low-level inversion. The periods of substantial weakening in our simulation are all associated with sustained low-level ascent, a rising inversion, and therefore strong cooling. This rising of the eye inversion with weakening was noted by Willoughby (1998) to be a fairly common (though not ubiquitous) characteristic of observed tropical cyclones. Kossin and Eastin (2001) presented observational evidence that tropical cyclones often transition between two distinct thermodynamic and kinematic regimes near the end of periods of intensification. In regime 1 (intensifying), vorticity and θ_e are highest in the eyewall and the eye is very dry, whereas in regime 2 (often after peak intensity), vorticity is nearly constant within the eye/eyewall (solid-body rotation), tangential winds increase within the eye, and the (low-level) eye moistens. Kossin and Eastin found that this regime transition could be caused by horizontal mixing between the eye and eyewall as a result of barotropic instability (Schubert et al. 1999). Examining profiles of vorticity, tangential wind, and θ_e (not shown), it does appear that some (but not all) aspects of the regime transition do occur on days 4 and 6 in our simulation. At the same time, it is clear from the budget that the mean vertical advection is responsible for a large portion of the cooling during these periods.

Therefore, we do not believe that mixing events are directly responsible for the rising of the inversion in our simulation.

At the beginning of RI, when the storm is still weak ($V_{\max 10} < 40 \text{ m s}^{-1}$), the greatest warming comes not from mean subsidence (as there is actually ascent in this region over a 12–18-h period), but rather from the divergence of the radial eddy flux of θ (RADVE), which is maximized at midlevels. We showed that the eddy fluxes are likely a consequence of a wavenumber-1 instability (Nolan et al. 2001). It is unclear if the importance of the radial eddy fluxes in driving warming of the eye holds more generally, as we have examined only a single simulation and in an idealized environment. Nevertheless, we have shown that the maximum warming does not need to be collocated with the maximum vertical advection, and that net warming can occur where there is mean ascent.

During the latter part of RI, RADVE becomes less important, and the mean vertical advection (VADVM) is responsible for warming the eye. Mean descent tends to be maximized in the upper troposphere (12–13 km, Fig. 9), whereas VADVM is maximized in the mid-troposphere (4–6 km). This is because the static stability is very small from 8- to 13-km heights (not shown), and so it is difficult for descent to lead to large warming. There exists a relative maximum in static stability in the midtroposphere, and so smaller vertical velocities can lead to relatively large warming (although there is a relative maximum in descent as well for at least part of this period). The tropospheric stability structure is largely a consequence of the existence of a similar profile in the mean tropical environment, but the maxima/minima are accentuated by the structure of the warm core itself (e.g., stability is decreased where net warming decreases with height). Stability rapidly increases with height above 13 km in the base of the tropical tropopause layer, and so the presence of weaker (compared to that at 12 km), yet still significant, descent at 14 km leads to the secondary upper-level maximum in warming.

As intensification proceeds, VADVM becomes increasingly concentrated along the eye/eyewall interface, owing to the localization of mean descent just inward of the eyewall. While the θ tendency from vertical advection becomes small or reverses sign in the interior of the eye during periods of quasi-steady state or weakening, the tendencies remain large and positive at the interface, as the strength of this zone of descent is mostly a function of the intensity itself. In general, the warming tendency in this region is entirely cancelled by diabatic cooling and mean radial advection (consistent with the results of ZLY02). The Doppler radar studies of

Guimond et al. (2010) and Heymsfield et al. (2001) have speculated that observations of individual strong downdrafts ($\sim 5\text{--}10\text{ m s}^{-1}$) along the eye/eyewall interface during periods of intensification (and rapid warming of the eye) imply that the warming of the eye is a direct result of these downdrafts. Our results are not consistent with this hypothesis, as much of the warming in our simulation is a result of weak mean subsidence, and the large downdrafts along the interface do not yield substantial warming.

Schubert et al. (2007) examined theoretically how certain distributions of inertial stability allowed for descent to be much larger at the edge of the eye than near the center. They found that this should occur for large eyes and/or intense storms, and that this leads to temperature being maximized away from the center. While our results support this “warm ring” hypothesis, our simulation also indicates that for a vortex exceeding a relatively weak intensity threshold, descent is almost always much stronger at the edge of the eye than at the center. Confirmation of this requires the examination of additional simulations, but we suspect that for realistic vortices, the mean vertical advection will generally act toward the creation of a warm ring structure throughout the troposphere. It is the negative tendencies from HDIF, RADVM, and HEAT that prevent this structure from occurring at most heights. A warm ring structure is indeed present from 1- to 4-km heights at and after day 5 in our simulation, and we believe this is largely because there is frictionally induced ascent (and cooling) near the center at low-levels.

Somewhat surprisingly, subgrid-scale horizontal diffusion has a large influence on the temperature changes both at the eye/eyewall interface and well inside the eye. Once the intensity exceeds about 50 m s^{-1} (regardless of intensity trend), the diffusive cooling tendency is of the same magnitude as advective warming tendencies. The spatial pattern of HDIF is often quite similar to that of VADVM, thereby preventing net warming from being maximized away from the center. During some periods of weakening, it is HDIF that dominates the cooling of the low- to midtropospheric eye above the inversion. Significant HDIF near the center is restricted to heights below about 8 km, and this partially explains why the maximum warming is often found in the upper troposphere during periods of quasi-steady state or weakening. The importance of horizontal diffusion on the temperature structure of the eye is a new finding, as far as we are aware. It is consistent however, with the recent study of Bryan and Rotunno (2009), which showed that the maximum intensity in axisymmetric simulations is very sensitive to the strength of the horizontal diffusion. Given that horizontal diffusion is

a parameterization of the effects of unresolved turbulence, the true importance of such turbulence on the structure of the warm core, and the realism of our simulation in this respect, remains highly uncertain.

We conclude this study by discussing what we still do not know: the true mean height of the maximum perturbation temperature and the degree to which this height varies in real tropical cyclones. While our simulations indicate that a midlevel primary maximum and (occasional) upper-level secondary maximum is most likely, it remains possible for a single maximum in perturbation temperature to occur, and for that maximum to be at upper levels, depending on the vertical profiles of static stability and mean descent. While the vertical structure of stability in the mean tropical troposphere is well known, we simply have no knowledge of whether the vertical structure of vertical velocity in our idealized simulations is representative of real tropical cyclones. We will further investigate the structure and variability of descent in the eye of simulated tropical cyclones in Part II of this study. While there is little hope of doing the same for real storms, we may soon be able to answer the question of where the warm core is typically maximized in such storms, from advances in microwave instruments (Brown et al. 2007), and from the high-altitude release of dropsondes from unmanned aerial vehicles.

Acknowledgments. The authors thank David Nolan for helpful discussions. The authors also are grateful for the helpful reviews of Jonathan Vigh, Jason Sippel, and one anonymous reviewer. This research was partially supported by ONR (Grant N000140910526), NOAA (HFIP), and the NSF (Grants 063064 and 0840651).

REFERENCES

- Braun, S. A., 2002: A cloud-resolving simulation of Hurricane Bob (1991): Storm structure and eyewall buoyancy. *Mon. Wea. Rev.*, **130**, 1573–1592.
- Brown, S., B. Lambrigtsen, A. Tanner, J. Oswald, D. Dawson, and R. Denning, 2007: Observations of tropical cyclones with a 60, 118, and 183 GHz microwave sounder. *Proc. IEEE Geoscience and Remote Sensing Symp.*, Barcelona, Spain, IEEE, 3317–3320.
- Bryan, G. H., and R. Rotunno, 2009: The maximum intensity of tropical cyclones in axisymmetric numerical model simulations. *Mon. Wea. Rev.*, **137**, 1770–1789.
- Dunion, J. P., 2011: Rewriting the climatology of the tropical North Atlantic and Caribbean Sea atmosphere. *J. Climate*, **24**, 893–908.
- Eliassen, A., 1951: Slow thermally or frictionally controlled meridional circulation in a circular vortex. *Astrophys. Norv.*, **5**, 19–60.

- Emanuel, K. A., 1986: An air-sea interaction theory for tropical cyclones. Part I: Steady-state maintenance. *J. Atmos. Sci.*, **43**, 585–604.
- Franklin, J. L., M. L. Black, and K. Valde, 2003: GPS dropwindsonde wind profiles in hurricanes and their operational implications. *Wea. Forecasting*, **18**, 32–44.
- Guimond, S. R., G. M. Heymsfield, and F. J. Turk, 2010: Multi-scale observations of Hurricane Dennis (2005): The effects of hot towers on rapid intensification. *J. Atmos. Sci.*, **67**, 633–654.
- Hack, J. J., and W. H. Schubert, 1986: Nonlinear response of atmospheric vortices to heating by organized cumulus convection. *J. Atmos. Sci.*, **43**, 1559–1573.
- Halverson, J. B., J. Simpson, G. Heymsfield, H. Pierce, T. Hock, and L. Ritchie, 2006: Warm-core structure of Hurricane Erin diagnosed from high-altitude dropsondes during CAMEX-4. *J. Atmos. Sci.*, **63**, 309–324.
- Hawkins, H. F., and D. T. Rubsam, 1968: Hurricane Hilda, 1964. Part II: Structure and budgets of the hurricane core on 1 October 1964. *Mon. Wea. Rev.*, **96**, 617–636.
- , and S. M. Imbombo, 1976: The structure of a small, intense Hurricane Inez 1966. *Mon. Wea. Rev.*, **104**, 418–442.
- Heymsfield, G. M., J. B. Halverson, J. Simpson, L. Tian, and T. P. Bui, 2001: ER-2 Doppler radar investigations of the eyewall of Hurricane Bonnie during the Convection and Moisture Experiment-3. *J. Appl. Meteor.*, **40**, 1310–1330.
- Holland, G. J., 1997: The maximum potential intensity of tropical cyclones. *J. Atmos. Sci.*, **54**, 2519–2541.
- Hong, S.-Y., and J.-O. J. Lim, 2006: The WRF single-moment 6-class microphysics scheme (WSM6). *J. Korean Meteor. Soc.*, **42**, 129–151.
- , Y. Noh, and J. Dudhia, 2006: A new vertical diffusion package with an explicit treatment of entrainment processes. *Mon. Wea. Rev.*, **134**, 2318–2341.
- Kepert, J. D., 2001: The dynamics of boundary layer jets within the tropical cyclone core. Part I: Linear theory. *J. Atmos. Sci.*, **58**, 2469–2484.
- Knaff, J. A., S. A. Seseske, M. DeMaria, and J. L. Demuth, 2004: On the influences of vertical wind shear on symmetric tropical cyclone structure derived from AMSU. *Mon. Wea. Rev.*, **132**, 2503–2510.
- Kossin, J. P., and M. D. Eastin, 2001: Two distinct regimes in the kinematic and thermodynamic structure of the hurricane eye and eyewall. *J. Atmos. Sci.*, **58**, 1079–1090.
- Kurihara, Y., 1975: Budget analysis of a tropical cyclone simulated in an axisymmetric numerical model. *J. Atmos. Sci.*, **32**, 25–59.
- , and M. A. Bender, 1982: Structure and analysis of the eye of a numerically simulated tropical cyclone. *J. Meteor. Soc. Japan*, **60**, 381–395.
- La Seur, N. E., and H. F. Hawkins, 1963: An analysis of Hurricane Cleo (1958) based on data from research reconnaissance aircraft. *Mon. Wea. Rev.*, **91**, 694–709.
- Liu, Y., D.-L. Zhang, and M. K. Yau, 1999: A multiscale numerical study of Hurricane Andrew (1992). Part II: Kinematics and inner-core structures. *Mon. Wea. Rev.*, **127**, 2597–2616.
- Nolan, D. S., M. T. Montgomery, and L. D. Grasso, 2001: The wavenumber-1 instability and trochoidal motion of hurricane-like vortices. *J. Atmos. Sci.*, **58**, 3243–3270.
- , Y. Moon, and D. P. Stern, 2007: Tropical cyclone intensification from asymmetric convection: Energetics and efficiency. *J. Atmos. Sci.*, **64**, 3377–3405.
- Pendergrass, A. G., and H. E. Willoughby, 2009: Diabatically induced secondary flows in tropical cyclones. Part I: Quasi-steady forcing. *Mon. Wea. Rev.*, **137**, 805–821.
- Powell, M. D., E. W. Uhlhorn, and J. D. Kepert, 2009: Estimating maximum surface winds from hurricane reconnaissance measurements. *Wea. Forecasting*, **24**, 868–883.
- Schubert, W. H., and J. J. Hack, 1982: Inertial stability and tropical cyclone development. *J. Atmos. Sci.*, **39**, 1687–1697.
- , M. T. Montgomery, R. K. Taft, T. A. Guinn, S. R. Fulton, J. P. Kossin, and J. P. Edwards, 1999: Polygonal eyewalls, asymmetric eye contraction, and potential vorticity mixing in hurricanes. *J. Atmos. Sci.*, **56**, 1197–1223.
- , C. M. Rozoff, J. L. Vigh, B. D. McNoldy, and J. P. Kossin, 2007: On the distribution of subsidence in the hurricane eye. *Quart. J. Roy. Meteor. Soc.*, **133**, 595–605.
- Shapiro, L. J., and H. E. Willoughby, 1982: The response of balanced hurricanes to local sources of heat and momentum. *J. Atmos. Sci.*, **39**, 378–394.
- Smith, R. K., 1980: Tropical cyclone eye dynamics. *J. Atmos. Sci.*, **37**, 1227–1232.
- Stern, D. P., 2010: The vertical structure of tangential winds in tropical cyclones: Observations, theory, and numerical simulations. Ph.D. dissertation, University of Miami, 455 pp. [Available at <http://etd.library.miami.edu/theses/available/etd-06242010-181136/>]
- , and D. S. Nolan, 2011: On the vertical decay rate of the maximum tangential winds in tropical cyclones. *J. Atmos. Sci.*, **68**, 2073–2094.
- , and —, 2012: On the height of the warm core in tropical cyclones. *J. Atmos. Sci.*, **69**, 1657–1680.
- Vigh, J. L., and W. H. Schubert, 2009: Rapid development of the tropical cyclone warm core. *J. Atmos. Sci.*, **66**, 3335–3350.
- , J. A. Knaff, and W. H. Schubert, 2012: A climatology of hurricane eye formation. *Mon. Wea. Rev.*, **140**, 1405–1426.
- Wang, Y., 2001: An explicit simulation of tropical cyclones with a triply nested movable mesh primitive equation model: TCM3. Part I: Model description and control experiment. *Mon. Wea. Rev.*, **129**, 1370–1394.
- Willoughby, H. E., 1990: Gradient balance in tropical cyclones. *J. Atmos. Sci.*, **47**, 265–274.
- , 1998: Tropical cyclone eye thermodynamics. *Mon. Wea. Rev.*, **126**, 3053–3067.
- Zhang, D.-L., Y. Liu, and M. K. Yau, 2002: A multiscale numerical study of Hurricane Andrew (1992). Part V: Inner-core thermodynamics. *Mon. Wea. Rev.*, **130**, 2745–2763.